Crater formation via homoepitaxy of adatoms dislodged from reducing oxide islands on metal surfaces

Guangwen Zhou,[1,*] Weiying Dai,[2] and Judith C. Yang[3]
[1]*Department of Mechanical Engineering & Multidisciplinary Program in Materials Science and Engineering, State University of New York, Binghamton, New York 13902, USA*
[2]*MR Physics Center, Department of Radiology, Harvard University, Massachusetts 02215, USA*
[3]*Department of Mechanical Engineering and Materials Science, University of Pittsburgh, Pennsylvania 15261, USA*
(Received 28 April 2008; published 19 June 2008)

The reduction of Cu_2O islands on Cu(100) surfaces under vacuum annealing leads to the formation of surface craters on the substrate surface surrounding the reducing oxide islands. These craters exhibit growth instability characterized by increased slope of both the inner and outer facets of the crater rims. We suggest that the crater formation and the growth instability are related to the homoepitaxial growth of Cu adatoms dislodged from the reducing Cu_2O islands. Incorporation of such atomic processes in kinetic Monte Carlo simulations reproduces the morphological features of the experimentally observed craters.

DOI: 10.1103/PhysRevB.77.245427 PACS number(s): 68.35.bd, 68.35.Fx, 68.37.Lp, 68.37.Ps

I. INTRODUCTION

The reduction of metal oxides plays critical roles in many fields including materials science, microelectronics, and chemical applications.[1–3] While the reaction equation is simple (in the case of cuprite, it is $Cu_2O \rightarrow Cu + O_2$), many aspects of the reaction still remain poorly understood. Traditionally, the reduction process has been described using phenomenological kinetic models (e.g., "nucleation and growth model" and "interface model") where the new phase, i.e., the reduced oxide, nucleates and grows on the surface of the parent oxide and the reaction rate depends either on the initial nucleation rate of new phase or on the area of the interface between the reduced phase and the parent oxide phase.[1,3,4] Although these models have been found useful in the description of the reduction process of many metal oxides including oxide single crystals and bulk oxide powders,[5–10] here we show that they do not apply to the reduction of surface oxide islands. Our *in situ* transmission electron microscopy (TEM) and atomic force microscopy (AFM) observations of the reduction of Cu_2O islands on Cu(100) surfaces reveal that the reduction of these oxide islands is accompanied by the growth of the reduced phase (e.g., Cu) on the substrate surface surrounding the oxide islands rather than on the parent oxide; this is fundamentally different from the assumption by the phenomenological kinetic models. We show that the reduction of these surface oxide islands by this mechanism leads to the formation of surface craters (Fig. 1) and the growth of the crater rim is controlled by the homoepitaxial growth of Cu adatoms displaced from the reducing Cu_2O islands.

II. EXPERIMENTAL DETAILS

Our experiments were carried out in a modified JEOL 200CX TEM equipped to allow observation of oxidation and reduction under controlled gas environments.[11] Cu(100) single-crystal films were grown on irradiated NaCl(100) by sputter deposition. The Cu films were removed from the substrate by floatation in de-ionized water, washed and mounted on a specially prepared TEM specimen holder that allows for resistive heating. Any native Cu oxide is removed by annealing the films in the TEM under vacuum conditions at ~750 °C,[12] resulting in clean copper surfaces. The experiments involve two steps: (i) creation of epitaxial Cu_2O islands on Cu(100) by *in situ* oxidation of Cu(100) surfaces inside the TEM, and (ii) reduction of the Cu_2O islands by vacuum annealing. The first step has been extensively discussed in our previous work.[13–17] The reduction experiments were carried out by *in situ* annealing of the oxidized Cu films inside the TEM under vacuum conditions ($\sim 8 \times 10^{-8}$ Torr) at ~800 °C. Thereafter, the surface morphology was analyzed by *ex situ* AFM at room temperature.

III. RESULTS AND DISCUSSION

Figure 2 is a BF (bright field) TEM micrograph showing the morphology of the Cu film with partially reduced Cu_2O islands, where the oxide islands were reduced for ~2 min at 800 °C under vacuum. The reduction of Cu_2O results in solid Cu and O_2 gas. The oxygen desorbs from the surface due to the high-vacuum conditions as well as the small solubility of oxygen in bulk copper.[18,19] The occurrence of the dark contrast around the oxide islands is due to the formation of the reduced phase (Cu) layer on the substrate surface, as

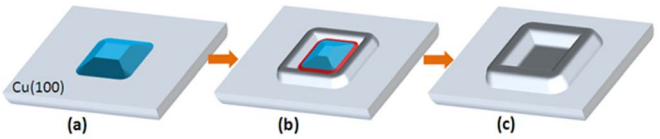

FIG. 1. (Color online) Proposed mechanism for the crater formation via reduction of surface oxide islands: (a) one Cu_2O island on a Cu(100) surface, (b) reduction of the oxide island leads to the homoepitaxy of the reduced phase (e.g., Cu) on the substrate surface surrounding the reducing oxide island, where Cu_2O dissociation occurs at the three-phase (metal-vacuum-oxide) contact line (marked by the red line), (c) formation of the surface crater after the complete reduction of the oxide island.

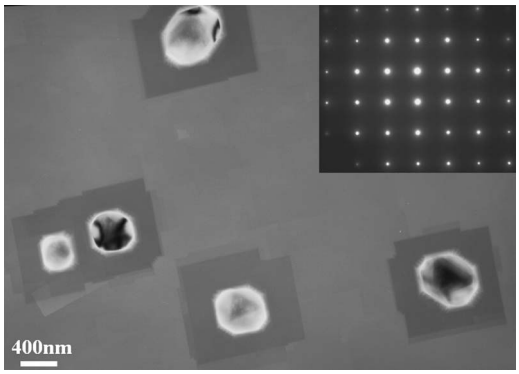

FIG. 2. Bright field TEM image of Cu(100) after an initial reduction of the oxide islands at 800 °C under vacuum, the occurrence of dark contrast in the area surrounding the reducing oxide islands is due to the homoepitaxial growth of Cu overlayer. The newly formed Cu overlayer and the bare Cu area have identical electron-diffraction pattern of copper (inset), suggesting the homoepitaxial growth of the Cu overlayer during the oxide reduction.

confirmed by selected area electron diffraction (SAD). The thickness of the newly formed Cu overlayer is ~10 nm, as determined from AFM images of partially reduced Cu_2O islands. Interestingly, the reduction of the oxide islands results in the growth of the reduced phase on the substrate surface around the oxide islands, rather than filling up the space left by the oxide. The fourfold symmetry of the newly formed Cu overlayer is related to the (100) orientation of the Cu substrate. The newly formed Cu overlayer (e.g., the regions with dark contrast) and the adjacent bare Cu area give identical electron-diffraction pattern (the inset in Fig. 2), revealing the homoepitaxial growth of the Cu overlayer on the Cu(100) substrate surrounding the reducing Cu_2O islands.

The Cu(100) surfaces can be oxidized at different oxidation temperatures, leading to the formation of oxide islands with different morphologies.[14,15] Figure 3 shows some atomic force microscopy (AFM) images of the oxide islands formed at the different oxidation temperatures and the surface topology of the Cu surfaces after the oxide islands are reduced. The AFM observations indicate that the reduction

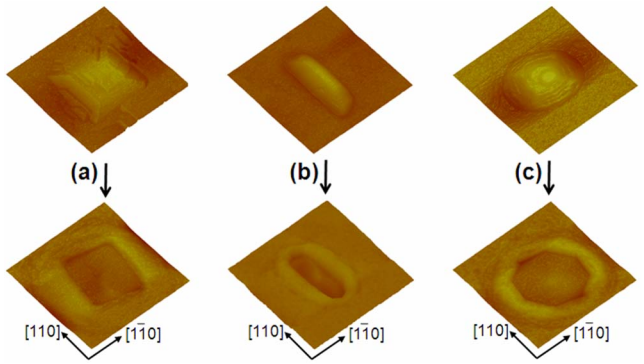

FIG. 3. (Color online) Representative AFM images of the oxide islands formed at different oxidation temperatures (a) 500, (b) 600, and (c) 750 °C, and the surface morphology of the Cu film after the reduction reaction at 800 °C under vacuum (5×5 μm^2, z range: 0.15 μm).

of the oxide islands leads to the formation of craters on the Cu surfaces and the craters take the shapes that are correlated with the morphology of the oxide islands before their reduction. The craters are faceted along the inner and outer walls of their rims. The height of the crater rim is roughly constant for each crater but varies among different craters, ranging from 45 to 70 nm. The AFM observations indicate that the craters have a relatively constant rim width of 550 ± 50 nm, which can also be noted from the contrast feature of the TEM images as shown in Fig. 2. Line-profile analysis of these craters along the principal crystallographic direction of $[1\bar{1}0]$ reveals that the outer facets form angle α varying from 10° to 35° and the inner facets form angle β ranging from 20° to 60° with respect to the base plane along $[1\bar{1}0]$ direction, but $\alpha<\beta$ within the same crater. The definition of the contact angle of α and β is given in Fig. 4(b).

One of the most intriguing features of these craters is the presence of tall rims around the craters. We first stress that, unlike the three-dimensional (3D) faceted structures in heteroepitaxial systems, the formation of the crater rims in the present homoepitaxial system cannot be attributed to epitaxial stress and should be kinetic in nature. The formation of large heights of the crater rims involves the transfer of Cu atoms dislodged from the reducing Cu oxide island to its adjacent growing crater rim. Our earlier work revealed that the oxide island perimeter along the three-phase (metal-vacuum-oxide) contact line, as marked by the red line in Fig. 1(b), is the preferred sites for the oxide reduction because these sites provide the easiest pathway for transport and crystallization of the reduced phase of Cu onto the adjacent area of the Cu substrate.[12] Since the oxide dissociation occurs at the island bottom, the homoepitaxial growth of the crater rim must call for upward adatom diffusion from the crater bottom onto the top of the growing rim. Another striking feature of these craters is the asymmetrical slope evolution of the inner and outer facets of the crater rim. The inner facet angle β is steeper than the outer facet angle α for each crater, implying different kinetic processes along the inner and outer facets of the crater rim.

We use kinetic Monte Carlo simulations to gain a microscopic understanding of the homoepitaxial growth of the crater rim during the reduction of the oxide islands. The basic processes included in the model are shown in Fig. 4(a). The Cu homoepitaxy is initiated by the surface diffusion of Cu adatoms dislodged from the reducing island. Surface migration of the adatoms is modeled as a nearest-neighbor hopping process at the rate, $k(E,T)=\upsilon_0\exp(-E/k_BT)$, where E is the hopping barrier, T the substrate temperature, and k_B Boltzmann's constant. The attempt frequency υ_0 is $\upsilon_0=k_BT/h=4.2\times10^{10}T$, with h Plank's constant, and T given in degrees Kelvin. The hopping barrier is composed of a substrate term E_S, a contribution E_N from each in-plane nearest neighbor, and the step-edge barrier E_B, i.e., $E=E_S+nE_N+(m_i-m_f)E_B$, where n is the number of in-plane nearest neighbor before the hop, m_i and m_f are the number of the next-nearest neighbors in the planes beneath and above the hopping atom before (m_i) and after (m_f) a hop, respectively.[20–22] The barrier E_B has a nonzero value only if $m_i>m_f$ and its effect is to make adatoms difficult to approach the step-edge sites.[21] If a

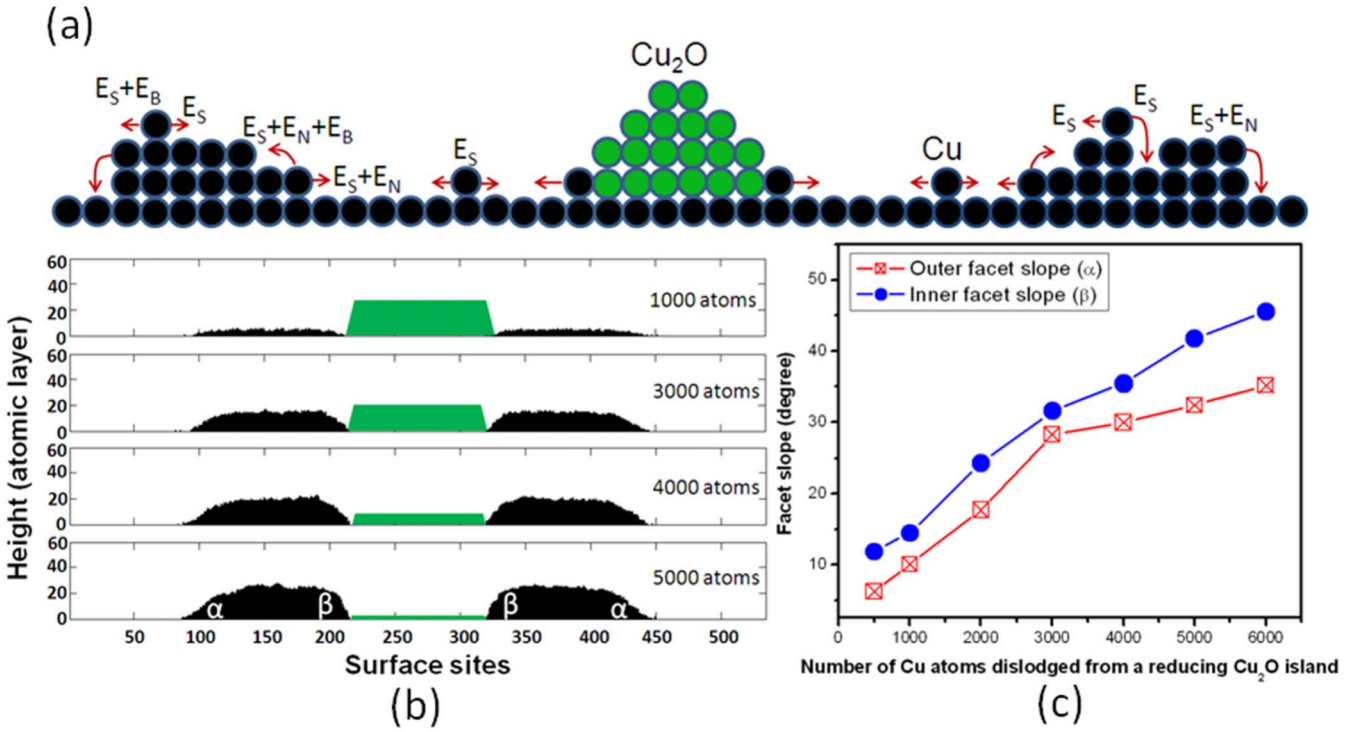

FIG. 4. (Color online) (a) One-dimensional illustration of the simulation model we use, where the growth of the crater rims is related to the homoepitaxy of Cu adatoms dissociated from the reducing Cu_2O island at the island bottom corners; (b) KMC simulations of the crater formation via homoepitaxial growth of Cu at 800 °C, α and β are the contact angle of the outer and inner facet with respect to the substrate, respectively. The reduction of the Cu_2O island is schematically shown at the center of the substrate as an eye guidance; (c) Slope evolution of the inner and outer facets of the rim measured from the KMC simulations.

site has two atoms as its nearest neighbors [(1+1)-dimensional growth], then the adatom sticks and occupies this stable site. Otherwise, it will diffuse to one of the nearest sites. Notice that the presence of the step-edge barrier depends on a hop direction and the number of the next-nearest neighbors both before and after the hop has to be considered in order to detect a step. The model parameters used are E_S=0.49 eV,[23] E_N=0.24 eV,[23] and E_B=0.27 eV,[24,25] as obtained from the self-diffusion of Cu adatoms on terraces and at edges and steps. The diffusion barriers for the different atomic processes are given in Table I.

The formation of the crater structure is observed from our (1+1)-dimensional KMC simulations. Figure 4(b) shows a few snapshots of the morphological evolution of the crater from the simulations. Several distinct features can be identified from these simulations. First, both the inner and outer walls of the crater rim show the faceting instability, as illustrated by the thickness dependence of the facet slope. The inner facet angle β is steeper than the outer facet angle α at each growth stage. Both α and β are observed to grow, but exhibiting different growth behaviors, as shown in Fig. 4(c). The simulations also reveal that there is a rapid increase in the rim height/width aspect ratio during the crater growth. The effect of reduction temperatures on the crater structure is also checked by KMC simulations.

TABLE I. Energy barriers $[E=E_S+nE_N+(m_i-m_f)E_B]$ in eV used in the kMC simulations. The details of the atomic processes are shown in Fig. 4(a).

	eV
Terrace diffusion (E_S)	0.49
Diffusion away from a step (E_S+E_N)	0.73
Diffusion to a step edge (E_S+E_B)	0.76
Descent at a step edge (E_S+E_N)	0.73
Ascent at a step ($E_S+E_N+E_B$)	1

Our model reproduces the morphological features of the experimentally observed craters such as steepening of the inner and outer facets, larger slope of the inner facet (e.g., $\beta > \alpha$), and the relatively constant rim width. As shown from the kinetic processes described in Fig. 4(a), the lateral growth of the crater rim depends on adatoms descending at steps along the outer/inner facets of the crater rim while the rim thickening is related to adatoms ascending along the inner facet. Such upward adatom diffusion is active whenever steps are present,[26] and it becomes more efficient as increasing the substrate temperature (here T=800 °C for the oxide reduction). This temperature effect can also be inferred from KMC simulations at different temperatures. As shown in Fig. 5, the contact angles become larger as increasing the growth temperature, suggesting an enhanced upward diffusion of adatoms at the higher temperatures. However, it is also noted from our *in situ* TEM observations that the temperature has to be greater than ~600 °C in order to have the reaction of

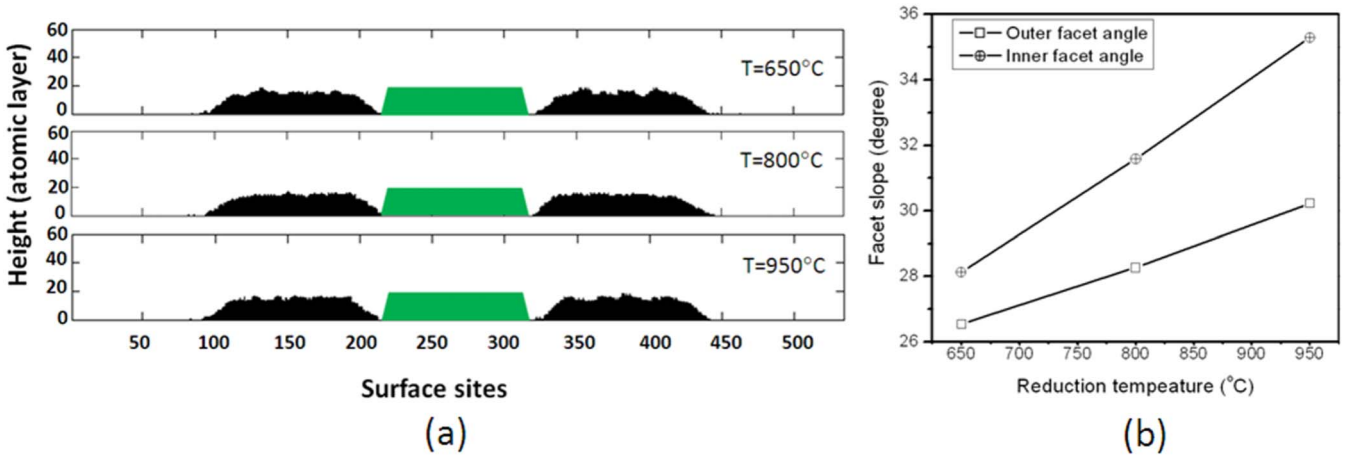

FIG. 5. (Color online) (a) Crater morphologies obtained from KMC simulations at different reduction temperatures but with the same number of Cu atoms (3000 atoms) supplied from a reducing Cu_2O island; (b) contact angle of the inner and outer facets measured from the KMC simulations at the different growth temperatures.

oxide reduction to occur, which limits the temperature range in the KMC simulations.

The steepening (i.e., unstable growth) of the rim facets as well as the relative constant rim width are related to the step-edge barrier (E_B) that hinders the rim lateral growth by preventing adatoms to diffuse over a step edge from an upper to a lower terrace.[27,28] The steepening of the outer facet (α) is only related to the descending processes of the adatoms while the steepening of the inner facet (β) depends on both the adatom descending and ascending, and β is larger than α due to the nonequilibrium uphill diffusion of the adatoms along the inner facet of the crater rim.

As can be noted in Fig. 4(c), the growth rate of the contact angles decreases with the continued deposition of Cu atoms, suggesting that the contact angles may become saturated at certain growth stage. It is indeed observed from KMC simulations that the inner contact angle saturates at ~65° with ~10000 atoms deposited. This is probably due to the increased number density of surface steps at the large contact angle, which makes the upward diffusion of Cu atoms less efficient and leads to the stabilization of the contact angles. For the reduction of very large-sized oxide islands, the contact angles may become saturated before the reduction of the oxide island is completed. For this situation, we speculate that the new Cu atoms reduced from the remaining part of the oxide island nucleate most likely on the surface of the reducing oxide island, which causes a transition of the reaction mechanism to the "nucleation and growth" or "interface" mechanism related to the reduction of bulk oxides, and the crater growth mechanism becomes inapplicable then.

Homoepitaxy has conventionally been modeled as the processes of adatoms "raining" down onto a growing surface and pyramidlike mound morphologies are usually observed. As deposition proceeds, the mounds grow bigger and steeper (i.e., unstable), and may ultimately reach a steady state characterized by an approximately constant mound angle due to the balance between an uphill current formed by the edge-step barrier[27–30] and a downhill current caused by the "downward funneling" effect[31–33] or formation of some specific side facets that favor upward diffusion of adatoms.[24,26,34,35] However, the growth of the crater rims by the Cu homoepitaxy does not involve the deposition of adatoms on the entire growing surface; alternatively, the adatoms are supplied from a confined Cu source at the crater center at the substrate surface [Fig. 4(a)]. These unusual kinetic processes lead to some new growth features such as the asymmetrical slope evolution of the inner and outer sidewalls of the crater rims. Such asymmetrical growth kientics may not occur for the regular homoepitaxy without shadowing effects, for example, the homoepitaxy under normal-incidence deposition.[20,21,36–38]

IV. CONCLUSIONS

We have shown that the reduction of Cu_2O islands on Cu(100) surfaces is accompanied by the growth of the reduced phase on the substrate surface surrounding the oxide islands rather than on the parent oxide, which is fundamentally different from the assumption by the phenomenological kinetic models related to the reduction of bulk oxides. The reduction of these surface oxide islands by this mechanism leads to the formation of surface craters and the growth of the crater rim is controlled by the homoepitaxial growth of Cu adatoms dislodged from the reducing Cu_2O islands. Since oxide island formation during oxidation has been observed in many other metals systems including Ni, Fe, Ti, Co, Pd, Ir, Sn, as well as in Cu, we expect such processes to be easily feasible in many metal systems by carefully choosing oxidation-reduction conditions.

*Corresponding author: gzhou@binghamton.edu

[1] B. Delmon, in *Handbook of Heterogeneous Catalysis*, edited by G. Ertl, H. Knozinger, and J. Weitkamp (Wiley, New York, 1997), p. 264.
[2] J. Li, J. W. Mayer, and K. N. Tu, Phys. Rev. B **45**, 5683 (1992).
[3] H. H. Kung, *Transition Metal Oxides: Surface Chemistry and Catalysis* (Elsevier, New York, 1989).
[4] C. H. Bamford, C. F. H. Tipper, and R. G. Compton, (Elsevier, New York, 1984), Vol. 21.
[5] J. A. Rodriguez, J. C. Hanson, A. I. Frenkel, J. Y. Kim, and M. Perez, J. Am. Chem. Soc. **124**, 346 (2002).
[6] J. Y. Kim, J. A. Rodriguez, J. C. Hanson, A. I. Frenkel, and P. L. Lee, J. Am. Chem. Soc. **125**, 10684 (2003).
[7] J. G. Chen, D. A. Fischer, J. H. Hardenbergh, and R. B. Hall, Surf. Sci. **279**, 13 (1992).
[8] R. P. Furstenau, G. Mcdougall, and M. A. Langell, Surf. Sci. **150**, 55 (1985).
[9] T. Ressler, R. E. Jentoft, J. Wienold, M. M. Gunter, and O. Timpe, J. Phys. Chem. B **104**, 6360 (2000).
[10] J. A. Rodriguez, J. Y. Kim, J. C. Hanson, M. Perez, and A. I. Frenkel, Catal. Lett. **85**, 247 (2003).
[11] M. L. McDonald, J. M. Gibson, and F. C. Unterwald, Rev. Sci. Instrum. **60**, 700 (1989).
[12] G. W. Zhou and J. C. Yang, Phys. Rev. Lett. **93**, 226101 (2004).
[13] G. W. Zhou, L. Wang, and J. C. Yang, J. Appl. Phys. **97**, 063509 (2005).
[14] G. W. Zhou and J. C. Yang, Phys. Rev. Lett. **89**, 106101 (2002).
[15] G. W. Zhou and J. C. Yang, Appl. Surf. Sci. **210**, 165 (2003).
[16] G. W. Zhou, W. S. Slaughter, and J. C. Yang, Phys. Rev. Lett. **94**, 246101 (2005).
[17] G. W. Zhou and J. C. Yang, J. Mater. Res. **20**, 1684 (2005).
[18] M. Hansen, *Constitution of Binary Alloys* (McGraw-Hill, New York, 1958).
[19] R. L. Pastorek and R. A. Rapp, Trans. Metall. Soc. AIME **245**, 1711 (1969).
[20] P. Smilauer and D. D. Vvedensky, Phys. Rev. B **52**, 14263 (1995).
[21] P. Smilauer, M. R. Wilby, and D. D. Vvedensky, Phys. Rev. B **47**, 4119 (1993).
[22] M. D. Johnson, C. Orme, A. W. Hunt, D. Graff, J. Sudijono, L. M. Sander, and B. G. Orr, Phys. Rev. Lett. **72**, 116 (1994).
[23] G. Boisvert and L. J. Lewis, Phys. Rev. B **56**, 7643 (1997).
[24] W. Zhu, F. B. de Mongeot, U. Valbusa, E. G. Wang, and Z. Zhang, Phys. Rev. Lett. **92**, 106102 (2004).
[25] The adatom ascending barrier at a monatomic-layer high step on Cu(100) surface is not readily available in the literature. Reference 24 gives an energy barrier of ~0.8 eV for adatom ascending on a Cu(110) surface. Since Cu(100) surface has a more compact structure than Cu(110), we therefore use a larger activation energy barrier, $E_S+E_N+E_B=1$ eV for adatom ascending at a monatomic step on Cu(100) surface, which produces a good agreement with the experimental observation.
[26] F. Buatier de Mongeot, W. G. Zhu, A. Molle, R. Buzio, C. Boragno, U. Valbusa, E. G. Wang, and Z. Y. Zhang, Phys. Rev. Lett. **91**, 016102 (2003).
[27] G. Ehrlich and F. Hudda, J. Chem. Phys. **44**, 1039 (1966).
[28] R. L. Schwoebel and E. J. Shipsey, J. Appl. Phys. **37**, 3682 (1966).
[29] S. C. Wang and G. Ehrlich, Phys. Rev. Lett. **70**, 41 (1993).
[30] J. G. Amar and F. Family, Phys. Rev. Lett. **77**, 4584 (1996).
[31] M. C. Bartelt and J. W. Evans, Phys. Rev. Lett. **75**, 4250 (1995).
[32] J. W. Evans, P. A. Thiel, and M. C. Bartelt, Surf. Sci. Rep. **61**, 1 (2006).
[33] J. W. Evans, D. E. Sanders, P. A. Thiel, and A. E. DePristo, Phys. Rev. B **41**, 5410 (1990).
[34] H. L. Yang, Q. Sun, Z. Y. Zhang, and Y. Jia, Phys. Rev. B **76**, 115417 (2007).
[35] K. Fichthorn and M. Scheffler, Nature (London) **429**, 617 (2004).
[36] J.-K. Zuo and J. F. Wendelken, Phys. Rev. Lett. **78**, 2791 (1997).
[37] S. van Dijken, L. C. Jorritsma, and B. Poelsema, Phys. Rev. B **61**, 14047 (2000).
[38] K. J. Caspersen, A. R. Layson, C. R. Stoldt, V. Fournee, P. A. Thiel, and J. W. Evans, Phys. Rev. B **65**, 193407 (2002).